Kinetic energy entrainment in wind turbine and actuator disc wakes: an experimental analysis

L.E.M. Lignarolo[1], **D. Ragni**[1], **C.J. Simão Ferreira**[1], **G.J.W. van Bussel**[1]
[1] Faculty of Aerospace Engineering, Delft University of Technology, Kluyverweg 1, 2629 HS Delft, The Netherlands

E-mail: l.lignarolo@tudelft.nl

Abstract. The present experimental study focuses on the comparison between the wake of a two-bladed wind turbine and the one of an actuator disk. The flow field at the middle plane of the wake is measured with a stereoscopic particle image velocimetry setup, in the low-speed Open Jet Facility wind tunnel of the Delft University of Technology. The wind turbine wake is characterized by the complex dynamics of the tip vortex development and breakdown. Analysis of the flow statistics show anisotropic turbulent fluctuations in the turbine wake, with stronger components in the radial direction. The wake of the actuator disc is instead characterized by isotropic random fluctuations. The mixing process in the shear layer is further analysed in terms of flux of mean flow kinetic energy, to show the main differences between the kinetic energy entrainment in the actuator and the turbine wake. This project is intended to provide the basis for understanding the origin of the limitations of the current wake models based on the actuator disc assumption.

1. Introduction

A common approach used to simplify the numerical simulation of the flow development in a wind farm is to model the single rotors as actuator discs. It is known from literature that this approach intrinsically misestimates the effects of flow turbulence, due to the absence of the blade flow and of its tip-vortex development and breakdown (Barthelmie et al, 2007). Consequently the mixing process across the wake interface and ultimately the rate at which the wake recovers the flow momentum is incorrectly modelled (Schepers, 2012). The accuracy of the flow simulation carried out with this simplification is generally acceptable in the far wake, region which is typically less affected by the presence of the rotating blades. With the current increase of rotors concentration in large off-shore and on-shore wind farms, an accurate simulation of the near-wake region has assumed increasing importance. Schepers (2012) explains how the strong velocity gradients at the wake edges of the actuator disc model cause unrealistic turbulence peaks enhancing the near-wake dissipation. Wu and Porté-Agel (2011) showed substantial flow discrepancies from the experimental and numerical results respectively up to the far wake of a wind turbine and an actuator disc wake. Despite the popularity of this simplified numerical model, few experimental studies are available, which analyse the flow field in the wake of an actuator disc. The numerical abstraction of an infinitely thin circular region, where body forces extract momentum from the wind flow can be reproduced in a wind tunnel via a porous disc which quickly dissipates the kinetic energy of the incoming flow into small-scale turbulence and, eventually, into heat. Aubrun et al (2013) and Aubrun et al (2007) used metal meshes for

manufacturing small-scale porous discs, while Medici (2005) and Sforza et al (1981) preferred perforated metal plates in contrast to wooden grids, as used by Pierella and Sætran (2010). A detailed, high-resolution 2D measurement of the flow in the wake a porous disc, including velocity field and turbulence statistics, is currently not available. The present experimental investigations analyses the different flow structures in the wake flow of a wind turbine (WT) and an actuator disc (AD). In particular, the studies aims to quantify the differences in the turbulent mixing. To the purpose the flow in the near and intermediate wake of a two-bladed small-scale WT and an AD is measured and compared. The two-dimensional three-component wake velocity field is measured with a stereoscopic particle image velocimetry setup (SPIV) in the low-speed Open Jet Facility (OJF) wind tunnel of Delft University of Technology. The WT model is the same two-bladed 60 cm diameter rotor used by the authors in Lignarolo et al (2014b), while the actuator disc is reproduced with a porous disc manufactured to match the diameter and drag coefficient of the WT. A double decomposition of the flow velocity field is employed to evaluate the kinetic energy transport in the flow. The mean flow kinetic energy fluxes at two wake locations (before and after the onset of the turbine wake instability) are compared with the ones obtained in the wake of the actuator disc. On the basis of the outcome of the present project, a further study on the origin of the limitations of the current wake models based on the actuator disc assumption will be possible.

2. Method

2.1. Experimental set-up and test conditions

Experiments have been conducted in the low-speed closed-loop open-jet wind tunnel located at the Aerodynamics Department of the Delft University of Technology. The OJF wind tunnel has an octagonal test section with an equivalent diameter of 3 m and a contraction ratio of 3:1, delivering a uniform stream with approximately 0.5% turbulent intensity up to 1 m from the nozzle (3×3 m^2 jet available) and lower than 2% at 6 m from the nozzle exit (2×2 m^2 jet available). A two-bladed horizontal-axis wind-turbine with a 0.6 m diameter has been designed for an optimal tip-speed ratio $\lambda = \omega\, r/U_\infty = 6$ and installed at approximately 1 rotor diameter from the tunnel exit. A larger distance from the nozzle would have been preferable, but this was not possible due to the fluctuations, caused by the jet instability, that happens 3 meters downstream. A detailed characterization of the wind-tunnel flow field, with an explanation of the above-mentioned instability phenomenon and more information on the wind turbine design can be found in Lignarolo et al (2014b). The wind turbine is operated in the present configuration at a free-stream wind velocity of $U_\infty = 4.7$ m/s, with a rotational speed of $\omega = 109.3$ rad/s (λ =6.97). At these conditions the maximum chord-based Reynolds number achieved is $Re_{ct} = 96{,}000$. A 60 cm diameter porous disc is manufactured by assembling of different layers of metal meshes having porosity $p = 60\%$, similarly to Aubrun et al (2013) and Aubrun et al (2007). In order to obtain the same wake expansion, the AD has been iteratively built to obtain the same thrust coefficient C_t of the WT. The final uniform disc with porosity $p = 32\%$ has been obtained by assembling of three layers of metal mesh. A six-component balance is used for measuring the thrust force on the turbine and on the disc, and results are presented in Section 3.1 with the uniform disc of porosity $p = 32\%$ matching the thrust coefficient of the WT at tip-speed ratio λ =6.97. A disc of uniform porosity has been used, neglecting the distribution of loads on the WT's blades. Section 3.2.1 contains a comparison between the direct method for calculating the thrust coefficient and an indirect method where the thrust is calculated from the measured velocity field by applying the momentum disc theory. Table 1 summarises the information about the experimental conditions. Stereoscopic PIV experiments are conducted to obtain the three-component velocity fields in the rotor wake; results are obtained via average of correlation maps, as detailed in Table 2.

A stereoscopic PIV setup has been installed on a traversing system able to scan the flow field in the wake of the horizontal-axis wind-turbine wake. The required illumination is provided by a Quantel Evergreen Nd:YAG laser system with an average output of 200 mJ/pulse. Two LaVision Imager Pro LX 16 Mpix (4870×3246 px^2, 12 bits) with pixel pitch of 7.4 μm/px are used to acquire images with a field of view of 0.297×0.227 m^2 (0.50×0.39 diameters). Laser and cameras are mounted on a traversing system able to translate in 2D of about 1.2 m × 0.9 m. The general setup is the same one used by Lignarolo et al (2014b) and shown in Figure 1. Ensemble of 200 unconditioned double-frame

recordings have been acquired and processed by LaVision Davis 8.1.4 to obtain vector fields with final interrogation windows of 24 × 24 px^2 with 50% overlap, having a resolution of 1.46 mm, and a vector spacing of 0.732 mm. Several vector fields are obtained in the wake of the WT and AD models up to 2.2 rotor diameters downstream, and further combined to form a total flow field as shown in section 3.

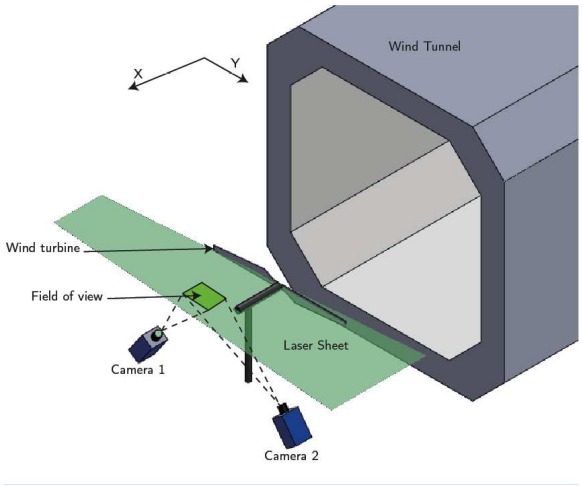

Figure 1. Wind tunnel schematic (Lignarolo et al, 2014b)

Table 1. Experimental parameters.

Parameters		**WT**	**AD**
Free-stream velocity	U_∞	4.7 m/s	4.7 m/s
Rotational frequency	ω	109.3 rad/s	-
Reynolds (chord based) blade root, r/*R* = 0.20	Re_{cr}	32,000	-
Reynolds (chord based) blade tip, *r/R* = 1	Re_{ct}	96,000	-
Reynolds (diameter based)	Re_D	188,000	188,000
Thrust coefficient	C_t	0.93	0.93
Tip speed ratio	λ	6.97	-

Table 2. System parameters of the stereoscopic PIV setup.

Parameters		**Stereoscopic PIV setup**	
Measurement field of view	*FOV*	297 × 227 mm^2	4870 × 3246 px^2
Interrogation window size	I_w	1.46 × 1.46 mm^2	24 × 24 px^2
Vector spacing	*S*	0.732 mm	12 px
Digital resolution	*DR*	16.40 px/mm	
Vectors	*N#*	404 × 270	

2.2. Theory

For each FOV, 200 random PIV samples are averaged in order to obtain time-average three-component velocity fields and turbulence statistics. A Reynolds double decomposition of the flow is applied as shown in (1), where $\overline{u_i}$ is the time average velocity in the *i*-direction and $u_{s,i}(t)$ is the time varying instantaneous fluctuation. The transport equation of the mean flow kinetic energy (2) is obtained as in Hamilton et al (2012), where $\overline{K_E}$ is the mean flow average kinetic energy, p is the pressure and $\overline{u'_i u'_j}$ are the Reynolds stresses. The last term of the right-hand-side of the equation represents the space gradient of the mean flow kinetic energy fluxes.

$$u_i(t) = \overline{u_i} + u_{s,i}(t) \tag{1}$$

$$\overline{u}_j \frac{\partial \overline{K_E}}{\partial x_j} = -\frac{\partial \bar{p}\overline{u}_i}{\partial x_i} - \left(-\overline{u'_i u'_j}\right)\frac{\partial \overline{u}_i}{\partial x_j} - \frac{\partial}{\partial x_j}\left[\overline{u}_i\left(\overline{u'_i u'_j}\right)\right] \quad (2)$$

As shown in Lignarolo et al (2014a) for i = 1 and j = 2, the term $\Phi = \bar{u}\left(\overline{u'v'}\right)$ represents the flux of streamwise mean flow kinetic energy in the radial direction, namely the entrainment of free-stream kinetic energy through the wake shear layer. The wake of the AD and of the WT are compared in terms of axial time-average velocity, three component of turbulence intensity, wake expansion and mean flow kinetic energy flux in two relevant locations.

3. Results

In this section the results of the experiments are shown. Time-average velocity fields, wake turbulence intensity in the rotor's and disc's wake will be compared. In the last paragraph the differences in the mixing processes in the wake of the turbine and of the actuator disc will pointed out.

3.1. Direct thrust measurements results

The results of the thrust measurements are reported in Figure 2: the black dots, fitted with the red curve, are results of the measurements performed by Lignarolo et al (2014b). For the design tip-speed ratio λ = 6 the thrust coefficient was C_t = 0.89. The blue dot is the results of the present measurements and represents both the thrust coefficient of the WT and the AD. For tip-speed ratio λ = 6.97 the thrust coefficient was C_t = 0.93

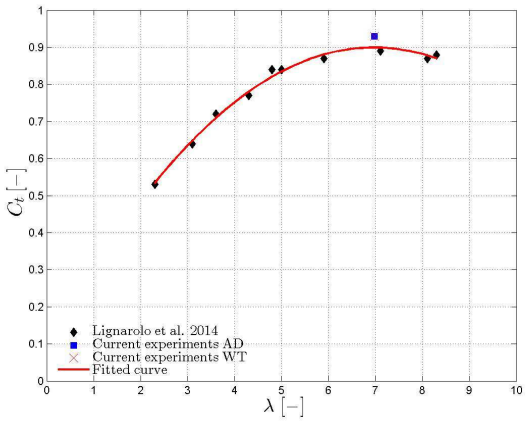

Figure 2. Thrust coefficient curve of the 2-bladed wind turbine model: comparison between old and present measurements

3.2. Global velocity field and indirect thrust calculation

In Figure 3 (left) the time-averaged wake normalised velocity fields $U^* = U/U_\infty$ are shown up to $x/D = 2.2$ downstream the rotor/disc location. From a first qualitative analysis, a localized increase of the wake shear layer thickness is visible starting from $x/D = 1.5$ downstream the turbine wake. This was demonstrated to be the sign of the development of the tip-vortex pairwise instability. For a tip-speed ratio λ = 6, in Lignarolo et al (2014b) the onset of the pairwise instability was located at $x/D = 1$ and it was shown the dependency of this phenomenon on the tip-speed ratio, namely earlier instability for higher tip-speed ratios. In the present experiments, when the system tower-nacelle-rotor was rebuilt, for a higher tip-speed ratio (λ = 6.97) the onset of the pairwise instability is at $x / D = 1.5$, contrary to what expected. This is ascribed to the sensitivity of the wake vortex system to any

disturbance in the flow/rotor boundary condition. In fact, the rebuilt tower-nacelle-rotor system of the present experiments may have differed slightly from the one of the previous campaign (Lignarolo et al, 2014b), introducing less perturbing vibrations and, eventually, causing a later instability. Figure 3 (right) shows the normalised velocity profiles $U^* = U/U_\infty$ at five different downstream locations. The graph demonstrates that the disc and the WT both generate wake with the same expansion rate (the wake border is considered as the locus of the points where the velocity is 99% of the free-stream velocity) as long as the same thrust coefficient is attained. The difference between the two wake expansion are within 3% (see Figure 4). This confirms that matching diameter and thrust coefficient are a sufficient condition for the two devices to develop the same wake expansion. At $x/D = 0.1$ the velocity profile in the AD wake shows evident oscillations compared to the WT wake velocity profile with $\Delta U/U_\infty = \mp 0.1$. This is ascribed to the different mechanism of wake generation. In fact, the AD is not responsible of any momentum exchange, while it dissipates the kinetic energy of the incoming flow into small-scale turbulence. As a matter of fact, as also evident in Figure 3, the very near wake of the AD is characterised by the presence of smaller wakes of the wire structures composing the disc, which are soon dissipated in the flow. As the second and third locations at $x/D = 0.8$ and $x/D = 1.1$ are still before the tip-vortex pairwise instability, a strong velocity gradient at the border of the WT wake is induced by the presence of the tip vortex. On the other side the AD wake shows a more continuous velocity variation. The mismatch between the WT and AD profiles drastically decreases after the instability location, where the tip vortex breaks down and the velocity gradient in the shear layer is less strong. The differences between the two velocity profiles are maximum in the inner wake, between $y/D = -0.1$ and $y/D = 0.2$, where the differences can reach up to $\Delta U = \mp 0.25 U_\infty$.

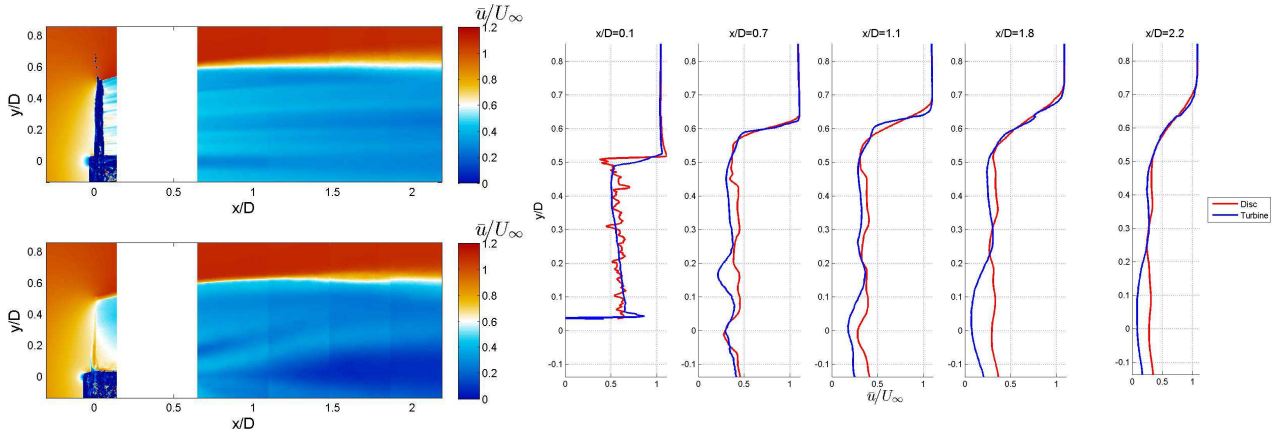

Figure 3. Axial velocity field in the wake of the AD (top left) and of the WT (bottom left). On the right, axial velocity profiles at five locations in the two wakes.

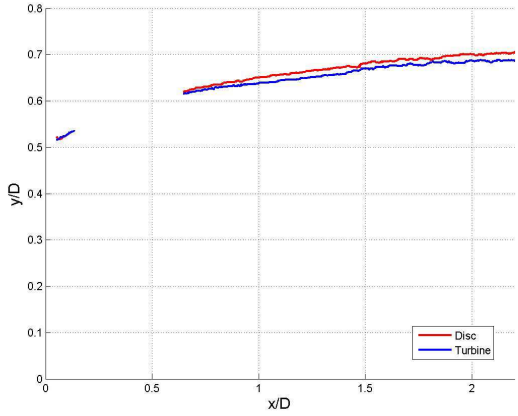

Figure 4. AD's and WT's wake expansion. The curves represent the loci of the points where the axial velocity is 99% of the free stream value.

3.2.1. Indirect calculation of thrust coefficient

From the velocity field, the thrust coefficient can be calculated indirectly via the momentum theory and compared to the value obtained with direct measurement via the 6-component balance. In this case, the thrust coefficient has been calculated using (3)

$$C_t = 4a\left(1-a\right) \tag{3}$$

where

$$a = 2\pi \int_{R_{root}}^{R_{tip}} \left[1-U^*\left(r, x=0\right)\right] r dr \cdot \frac{1}{A} \tag{4}$$

$$A = \pi\left(R_{tip}^2 - R_{root}^2\right) \tag{5}$$

The term $U^*(r, x = 0)$ is the radial distribution of normalized velocity at the rotor or disc location $x=0$. Since it was not possible to acquire PIV data at the disc location, because of the shadowing of the disc itself, the calculation is applied only to the turbine wake velocity field. The equality of the two devices thrust coefficient is ensured by the previous balance measurements. To correct for the distortion due to the presence of the passing blades, the velocity field is modified with a 2D linear interpolation of the data across the rotor location. The induction factor is calculated with (4) and it is equal to a = 0.388 for the WT and a = 0.376 for the AD, yielding respectively a thrust coefficient C_t = 0.949 and C_t = 0.938.

Table 3. Values of AD's and WT's thrust coefficient C_t obtained with direct balance measurements and by indirect calculation

Method	***Disc***	***Turbine***
Direct (balance)	0.930	0.930
From velocity field	0.938	0.949

3.3. Wake turbulence

In Figure 5 to 6 the time-average wake turbulence intensity in the *x*-, *y*- and *z*-directions is shown until 2.2D downstream past the rotor/disc location. The WT and AD wake turbulence profiles exhibit more

evident differences, compared to the velocity profiles in Figure 3, mainly the WT wake shows anisotropic turbulent fluctuations, contrarily to the isotropic ones of the AD wake turbulence. Figure 5 and Figure 6 present turbulence intensity in the *x*- and *y*-directions: both the AD and the WT profiles demonstrate a strong peak in turbulence intensity in correspondence of the wake shear layer, where most of the fluctuations are detected, but the WT exhibit a peak of streamwise fluctuations which is just 75% of the one in the radial direction. This does not hold for the AD wake, that shows a more isotropic turbulence behaviour. Already in previous literature about rotor wake aerodynamics it has been found out that the radial fluctuations are the most important ones (Cotroni et al, 2000; El Kasmi and Masson, 2008). Differences between WT and AD wake turbulence vanish downstream, after $x/D = 1.8$. Fluctuations in the out-of-plane (*z*-) direction in the WT wake are much weaker in the near wake region (until one diameter downstream) compared to fluctuations in the other two directions and differences between the WT and the AD wake turbulence are minor. This behaviour is attributed to the convection of the tip-vortex in the WT wake, which in the time-averaging process is accounted for as a turbulent fluctuation in the stream-wise and radial directions. In the intermediate-wake region, after the instability, the tip-vortices have broken down and diffused and, clearly, they are not present in the AD's wake. In the inner-wake region the mark of the WT's blades turbulence is very evident. In fact, in the WT's wake the turbulence intensity is always higher than the AD's wake turbulence: the turbulence generated by the AD is characterised by very small length scales and it decays extremely quickly (it almost completely dissipate within one rotor radius) whereas the turbulent structures generated by the rotor are self-sustaining.

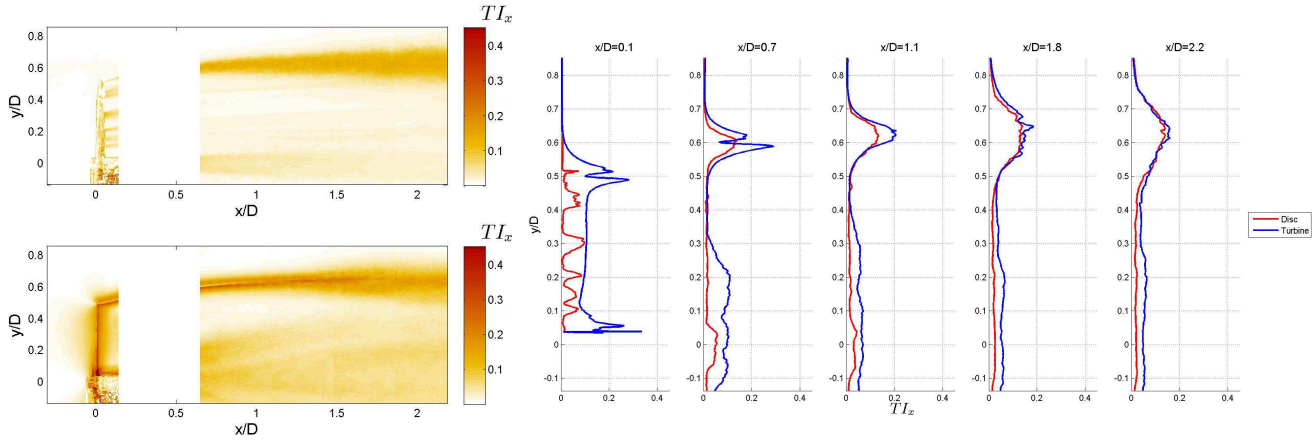

Figure 5. Turbulence intensity in the axial direction in the wake of the AD (top left) and of the WT (bottom left). On the right, axial turbulence intensity profiles at five locations in the two wakes.

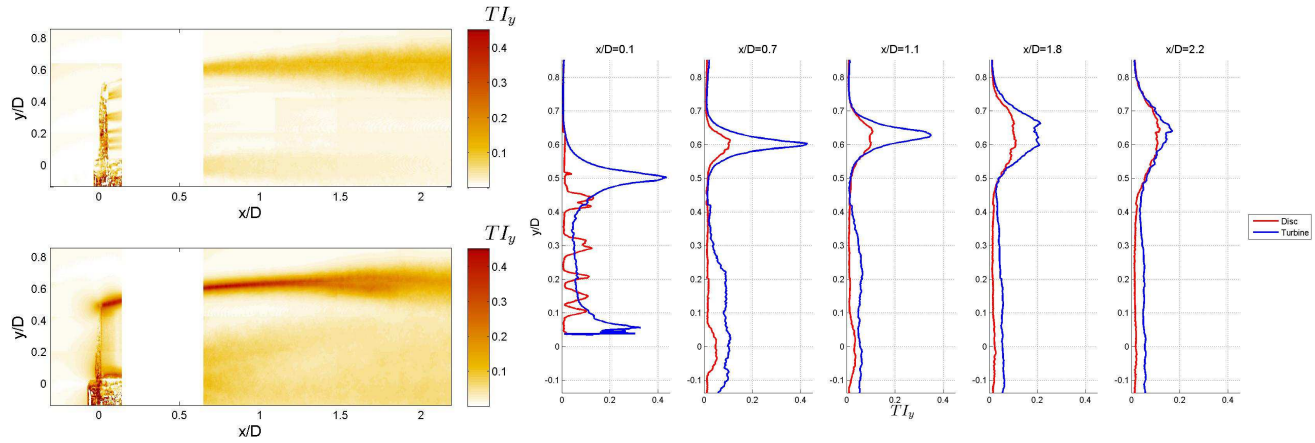

Figure 6. Turbulence intensity in the radial direction in the wake of the AD (top left) and of the WT (bottom left). On the right, radial turbulence intensity profiles at five locations in the two wakes.

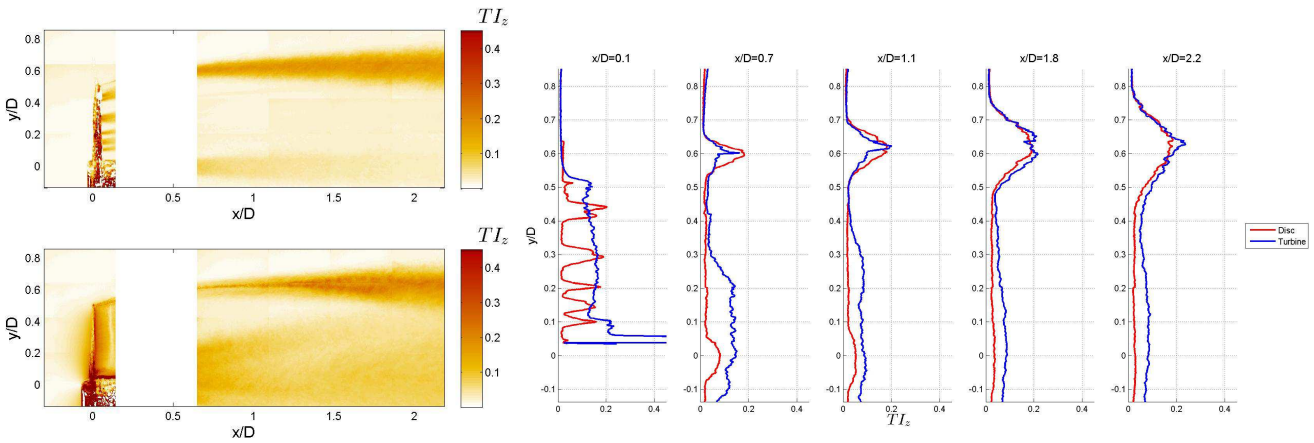

Figure 7. Turbulence intensity in the out-of plane direction in the wake of the AD (top left) and of the WT (bottom left). On the right, out-of plane turbulence intensity profiles at five locations in the two wakes.

3.4. Wake mixing

The analysis of the turbulence statistics in three directions does not provide complete information about the actual turbulent mixing in the wake shear layer. Figure 9 shows the radial profiles of the mean flow kinetic energy fluxes $\overline{\Phi}$ towards the inner part of the wake as described in section 2.2.

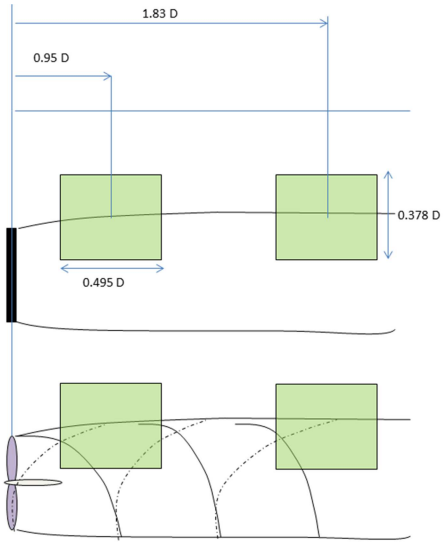

Figure 8. Measurement locations of the mean flow kinetic energy transport.

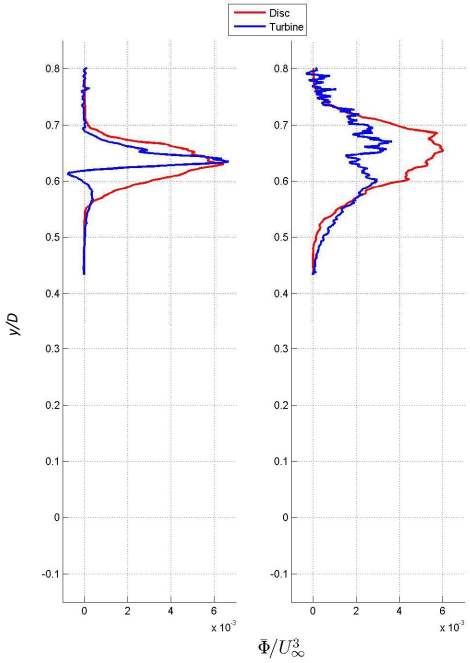

Figure 9. Mean flow kinetic energy transport at x/D = 0.95 and x/D = 1.83.

Measurements are performed at two downstream locations in the shear layer of the AD and WT wake as shown in Figure 8. The locations are in the near wake (before the tip-vortex instability) and in the intermediate wake (right after the tip-vortex instability), respectively centred at x/D = 0.95 and x/D = 1.83. Figure 9 shows that in the region within 1 diameter from the rotor, both the AD's and the WT wake exhibit a strong transport of mean flow kinetic energy, whose peaks reach the same values, despite the much higher value of the WT wake turbulence intensity in the same location, as evident in Figure 5 to 6. This is due to the strong velocity gradient that generates strong concentrated turbulence which promotes the transport. It must be considered that in the WT wake both random fluctuations and periodic vortices are accounted for as turbulence: nevertheless, Lignarolo et al (2014a) have demonstrated that the transport of kinetic energy due to the periodic vortical fluctuation is not leading to a net positive entrainment of energy in the WT wake. Comparing Figure 9a (left) and Figure 9b (right) shows that after the vortex breakdown caused by the pairing instability the strength of the kinetic energy transport in the WT wake collapses to about 50% of the original near-wake value, whereas it stays almost constant in the AD wake. The physical reasons for this phenomenon are to investigate.

4. Conclusions

The velocity field in the wake of 2-bladed 60 cm diameter wind turbine together with the one of a porous disc has been analysed by stereo particle image velocimetry. The analysis have shown that by matching the diameter and thrust coefficient, the two devices give rise to the same wake expansion (differences lower than 3%). Observation of turbulence statistics shows the isotropic behaviour of the AD wake turbulence and the evident anisotropy of the WT one, with higher fluctuations in the radial direction, confirming the findings of previous studies. Despite the turbulence intensity in the near wake of the WT is four times as large as the one of the AD wake, both wake exhibit the same value of mean flow kinetic energy flux in the near-wake shear layer. This quantity collapses to 50% of its

original value after the breakdown of the WT's tip-vortices caused by the pairwise instability. This demonstrates how the physics governing the turbulent mixing in the two wakes are intrinsically different. This detailed experimental comparison between the wake of a rotor and the one of a porous disc is intended to provide the basic knowledge about the different physics governing the two wake flows and, eventually, to constitute the basis for understanding the origin of the limitations of and improving the current wake models based on the actuator disc assumption.

References

[1] Aubrun, S., Devinant, P., Espana, G., 2007. Physical modelling of the far wake from wind turbines. Application to wind turbine interactions, in: Proceedings of the European Wind Energy Conference EWEC 2007.

[2] Aubrun, S., Loyer, S., Hancock, P.E., Hayden, P., 2013. Wind turbine wake properties: Comparison between a non-rotating simplified wind turbine model and a rotating model. Journal of Wind Engineering and Industrial Aerodynamics 120, 1-8

[3] Barthelmie, R.J., Frandsen, S.T., Nielsen, M.N., Pryor, S.C., Rethore, P.E., Jørgensen, H.E., 2007. Modelling and measurements of power losses and turbulence intensity in wind turbine wakes at Middelgrunden offshore wind farm. Wind Energy 10, 517-528.10.1002/we.238

[4] Cotroni, A., Di Felice, F., Romano, G.P., Elefante, M., 2000. Investigation of the near wake of a propeller using particle image velocimetry. Exp Fluids 29, S227-S236

[5] El Kasmi, A., Masson, C., 2008. An extended model for turbulent flow through horizontal-axis wind turbines. Journal of Wind Engineering and Industrial Aerodynamics 96, 103-122

[6] Hamilton, N., Kang, H.S., Meneveau, C., Cal, R.B., 2012. Statistical analysis of kinetic energy entrainment in a model wind turbine array boundary layer. Journal of Renewable and Sustainable Energy 4, 063105-063119

[7] Lignarolo, L.E.M., Ragni, D., Ferreira, C.S., van Bussel, G.J.W., 2014a. Experimental quantification of the entrainment of kinetic energy and production of turbulence in the wake of a wind turbine with Particle Image Velocimetry, 32nd ASME Wind Energy Symposium. American Institute of Aeronautics and Astronautics.

[8] Lignarolo, L.E.M., Ragni, D., Krishnaswami, C., Chen, Q., Simão Ferreira, C.J., van Bussel, G.J.W., 2014b. Experimental analysis of the wake of a horizontal-axis wind-turbine model. Renewable Energy (In press).http://dx.doi.org/10.1016/j.renene.2014.01.020

[9] Medici, D., 2005. Experimental Studies of Wind Turbine Wakes – Power Optimisation and Meandering, Mechanics. Royal Institute of Technology (KTH), Stockholm.

[10] Pierella, F., Sætran, L.R., 2010. Effect of initial conditions on flow past grids of finite extension, in: Proceedings of the 17th Australasian Fluid Mechanics Conference.

[11] Schepers, J.G., 2012. Engineering models in wind energy aerodynamics, Aerospace Engineering. Delft University of Technology.

[12] Sforza, P.M., Sheerin, P., Smorto, M., 1981 Three-Dimensional Wakes of Simulated Wind Turbines. AIAA Journal vol.19 (1101-1107)

[13] Wu, Y.-T., Porté-Agel, F., 2011. Large-Eddy Simulation of Wind-Turbine Wakes: Evaluation of Turbine Parametrisations. Boundary-Layer Meteorology 138, 345-366